CORE
Metadata, citation and similar papers at core.ac.uk
Provided by Digital.CSIC

Submitted, accepted and published by
Chemical Engineering Journal 2015, 269, 67-81

Redox Kinetics of $CaMg_{0.1}Ti_{0.125}Mn_{0.775}O_{2.9-\delta}$ for Chemical Looping Combustion (CLC) and Chemical Looping with Oxygen Uncoupling (CLOU)

A. Abad*, F. García-Labiano, P. Gayán, L. F. de Diego, J. Adánez

Instituto de Carboquímica (ICB-CSIC), Department of Energy and Environment,

Miguel Luesma Castán 4, Zaragoza 50018, SPAIN.

* Corresponding author. Tel.: +34 976 733 977. Fax: +34 976 733 318. E-mail address:

abad@icb.csic.es (Alberto Abad)

Submitted, accepted and published by
Chemical Engineering Journal 2015, 269, 67-81

Redox Kinetics of $CaMg_{0.1}Ti_{0.125}Mn_{0.775}O_{2.9-\delta}$ for Chemical Looping Combustion (CLC) and Chemical Looping with Oxygen Uncoupling (CLOU)

A. Abad*, F. García-Labiano, P. Gayán, L. F. de Diego, J. Adánez

Instituto de Carboquímica (ICB-CSIC), Department of Energy and Environment, Miguel Luesma Castán 4, Zaragoza 50018, SPAIN.

* Corresponding author. Tel.: +34 976 733 977. Fax: +34 976 733 318. E-mail address: abad@icb.csic.es (Alberto Abad)

Abstract

The objective of this study was to establish the kinetic of reactions involved in redox cycles of an oxygen carrier material based on a perovskite type structure with the formula $CaMg_{0.1}Ti_{0.125}Mn_{0.775}O_{2.9-\delta}$. The oxygen transport capacity and reactivity of this material during reduction with gaseous fuels (CH_4, H_2 and CO) and the subsequent oxidation with oxygen are studied in a TGA apparatus. Besides, the oxygen uncoupling properties of this material are analysed. Thus, kinetics for relevant reactions involved in Chemical Looping Combustion (CLC) and Chemical Looping with Oxygen Uncoupling (CLOU) were determined.

$CaMg_{0.1}Ti_{0.125}Mn_{0.775}O_{2.9-\delta}$ reactivity increased with the number of redox cycles, whereas the total oxygen transport capacity decreased from 8.5 to 8.0 wt.%. Particles that reached the maximum reactivity were denoted as "activated" material. Kinetics for both fresh and "activated" particles was determined. Conversion vs. time curves at different temperatures (973-1273 K), and reacting gas concentration (5-60 vol.% for CH_4, H_2 or CO; 5-21 vol.% for O_2) were obtained for both fresh and "activated"

material. For kinetics determination, the shrinking core model with control by chemical reaction and diffusion through the product layer was used to obtain the kinetic parameters.

Keywords

Chemical looping combustion (CLC); Chemical Looping with Oxygen Uncoupling (CLOU); Oxygen carrier; Manganese; Perovskite; Reaction kinetic.

1. Introduction

CO_2 capture and sequestration in fuel combustion processes is a relevant option in order to decrease the CO_2 emissions to the atmosphere [1]. Chemical Looping Combustion (CLC) has been identified as an interesting option in order to minimize the energy penalty related to the CO_2 capture process [2]. In CLC, a solid oxygen carrier transfer oxygen from the air to the fuel; so the combustion is carried out at absence of nitrogen. Therefore, the combustion process is shared in two steps, commonly carried out in two interconnected fluidized bed reactors; see Fig. 1. In the fuel reactor, the oxidation of the fuel happens and a highly CO_2 concentrated stream is obtained. Then, the oxygen carrier is reduced due to its oxygen lost; see reaction (1). Subsequently, the oxygen in air is taken from the reduced oxygen carrier in the air reactor; see reaction (2). The oxygen carrier is continuously circulating between the two reactors in order to supply a continuous flow of oxygen to support the fuel combustion.

$$(2n+m/2)\ M_xO_y + C_nH_m \rightarrow (2n+m/2)\ M_xO_{y-1} + n\ CO_2 + m/2\ H_2O \quad (1)$$

$$2\ M_xO_{y-1} + O_2 \rightarrow 2\ M_xO_y \quad (2)$$

Most of materials developed to be used as oxygen carrier are based on particulate matter composed by a metal oxide, which acts as the oxygen donor, mixed with an inert

material, which improves the mechanical performance of particles [3]. Recently, metal oxides with the capability to evolve gaseous oxygen at the fuel reactor conditions has been proposed as a way to improve the combustion rate of solid fuels in the so-called Chemical Looping with Oxygen Uncoupling (CLOU) process [4]. Materials based on copper and manganese have been proposed for CLOU [3-7]. It was demonstrated that the oxygen uncoupling property of CuO is of great importance in order to reach full combustion and high CO_2 capture rates in combustion of coal and biomass [8-11].
In addition, the oxygen uncoupling property could be of relevance to facilitate the complete combustion of gaseous fuels [12,13]. In this case, the oxygen carrier is reduced by decomposing in oxygen following reaction (3). Subsequently, the fuel is oxidized by the gaseous oxygen such as the homogeneous combustion with air; see reaction (4). However, for gaseous fuels both heterogeneous gas-solid reactions and oxygen uncoupling followed by homogenous oxidation of the fuel can be relevant as oxygen transference mechanism during fuel oxidation [14]. The relative relevance of every mechanism can depend on the experimental conditions, e.g. the fuel gas concentration or the relative reactivity of material in oxygen uncoupling and gas-solid reactions. The gaseous oxygen evolution from the oxygen carrier can be relevant when the fuel gas concentration is low or for low reactive materials with CH_4. In this case, the oxygen uncoupling property can be critical in order reach complete fuel combustion [15].

$$M_xO_y \rightarrow M_xO_{y-1} + 1/2\ O_2 \quad (3)$$

$$C_nH_m + (n+m/2)\ O_2 \rightarrow n\ CO_2 + m/2\ H_2O \quad (4)$$

Apart from metal oxide based particles, perovskite materials have also been identified as suitable materials as oxygen carriers considering the reversibility of the oxygen mobility in its structure [16,17]. Perovskite materials based on cheap metals have

received recently attention for fuel gas combustion in CLOU [18], e.g. manganese-calcium materials [19-20]. In this case, the addition of some metals, e.g. Mg or Ti, into the $CaMnO_{3-\delta}$ material improved the reactivity with a fuel gas [21]. Although this kind of materials are sulphur sensitive because of the presence of calcium [22], they can be suitable for combustion of clean gases, e.g. sweet natural gas. Recent results obtained with materials based on the $CaMnO_{3-\delta}$ perovskite are encouraging. Thus, the complete combustion of methane was obtained using a material with the stoichiometry $CaMn_{0.9}Mg_{0.1}O_{2.9-\delta}$ in different CLC units ranging from 0.5 to 140 kW_{th} [22-24], which improves results previously shown by Ni-based materials with high nickel content [25,26]. To get complete fuel combustion, the solids circulation flow-rate should be at least 10 times the minimum circulation value to supply the stoichiometric oxygen [22]. In fact, simulations performed with a theoretical model of the fuel reactor considering $CaMn_{0.9}Mg_{0.1}O_{2.9-\delta}$ as oxygen carrier showed that the oxygen uncoupling property of this perovskite was useful to improve the fuel conversion [15]. Theoretical model included kinetics of relevant reactions happening in the fuel reactor [27]. Thus, to take advantage of the oxygen uncoupling property, the fraction of oxygen released *via* oxygen uncoupling must prevail over oxygen transferred *via* gas-solid reaction. It is worth noting that the oxygen transport capacity of this material by oxygen uncoupling is $R_{OC,ou}$ = 1.1 wt.%, which is ten times lower than the total oxygen transport capacity when the material reacted with a fuel gas, which is $R_{OC,t}$ = 10.5 wt.% [27].

Recently, a similar material, i.e. $CaMn_{0.775}Mg_{0.1}Ti_{0.125}O_{2.9-\delta}$ has been proposed as an alternative to $CaMn_{0.9}Mg_{0.1}O_{2.9-\delta}$ [28]. $CaMn_{0.775}Mg_{0.1}Ti_{0.125}O_{2.9-\delta}$ showed improved performance in CLC units compared to $CaMn_{0.9}Mg_{0.1}O_{2.9-\delta}$ when fluidization behaviour, perovskite stability during repeated redox cycles and CH_4 conversion is considered [24,29].

Modelling of a CLC unit with $CaMnO_{3-\delta}$ based materials has shown to be a power tool in order to identify the most relevant processes converting fuel [15], i.e. *via* oxygen uncoupling or gas-solid reaction. The use of proper kinetics data for oxygen carrier reduction with reducing gases is required to predict the fuel reactor performance by mathematical modelling. Moreover, the oxidation kinetics is relevant in order to evaluate the oxidation degree reached in the air reactor.

The objective of this study was to determine the kinetics of both reduction and oxidation reactions taking place in the CLC process with the promising $CaMn_{0.775}Mg_{0.1}Ti_{0.125}O_{2.9-\delta}$ particles. The selected material was studied in a thermogravimetric analyser (TGA) apparatus analysing its reactivity with CH_4, H_2 or CO as reducing gases and O_2 for the oxidation reaction. The effect of temperature and gas concentration over the reaction rate was examined. In addition, the oxygen uncoupling kinetics was determined in a N_2 environment.

2. Experimental

2.1. Material

$CaMn_{0.775}Mg_{0.1}Ti_{0.125}O_{2.9-\delta}$ particles were manufactured by VITO (Flemish Institute for Technological Research, Belgium) using the spray drying method [28]. Particles prepared by spray drying were subsequently sintered at 1623 K for 4 h. The temperature of interest in the chemical looping process is in the 1150-1300 K interval. So, reacting temperature does not exceed the sintering temperature, and major modification into the solids due to a thermal process is not expected during normal CLC operation. Size fraction from 125 to 200 μm was used for kinetic determination. More information about this material can be found elsewhere [29].

2.2. Experimental setup

The reactivity and the oxygen transport capacity of $CaMn_{0.775}Mg_{0.1}Ti_{0.125}O_{2.9-\delta}$ material were determined in a TGA CI Electronics Ltd. Every experimental condition was evaluated starting with a new fresh sample. About 50 mg of oxygen carrier particles were loaded on a platinum holder, and a gas flow of 25 L/h (STP) was fed. The sample holder is a wire mesh platinum basket in order to minimize diffusional effect on the measured reaction rate. More information about the TGA set-up and procedure can be found elsewhere [30-32].

Reduction with CH_4, H_2 and CO, and oxidation with O_2 of the oxygen carrier were carried out by exposing the sample to CH_4, H_2, CO or O_2 diluted in nitrogen. 20 vol.% H_2O and 20 vol.% CO_2 was used during reduction with CH_4 and CO, respectively, in order to avoid carbon formation. Oxygen-nitrogen mixtures are used during the oxidation period. Also, the oxygen release rate -as gaseous O_2- of fully oxidized material was studied in an inert environment using high purity N_2. Experiments both at a programmed temperature and at a fixed temperature were carried out.

2.2.1. Temperature programmed experiments

The oxygen carrier sample was heated to 573 K in air atmosphere. No reaction occurred during this pre-heating step. After reaching this temperature the desired gas composition was introduced to the reactor and the temperature was increased up to 1273 K at a constant rate of 20 K/min. The weight loss was recorded in three different environments: highly pure N_2, 15 vol.% H_2 and 15 vol.% CH_4.

2.2.2. Fixed temperature experiments

For experiments at fixed temperature, the oxygen carrier sample was heated to the desired temperature in air atmosphere. After reaching the set temperature, the

experiment started by exposing the oxygen carrier to alternating reducing and oxidizing conditions.

To evaluate the stability of perovskite structure with the redox cycle number, three series of ten redox cycles each were carried out at 1173 K. The redox cycles were carried out alternating N_2, reducing gas and air. Every redox cycle starts with the oxygen carrier fully oxidized. The first step of the redox cycle consists in gaseous oxygen release in nitrogen environment for 300 s. After that, the reduction period with 15 vol.% H_2 or CH_4 started. The time for the reducing period was different in each series (20, 90 or 600 s), thus reaching different conversion of solids. In order to prevent the fuel and air mixing, a nitrogen flow was passed after reducing processes for 150 s. Finally, the sample was completely oxidized by air for 180 s. and further was reduced in 15 vol.% H_2 before the subsequent oxidation period. Thus, the conversion degree in the second experimental series was higher than that in the first one.

To obtain the conversion vs. time curves necessary for the kinetic determination, five redox cycles were carried out alternating reducing and oxidising conditions. The inert period before reduction period was 10 s in order to minimize the decomposition of the oxygen carrier before the reaction with the fuel gas. A variation of reactivity with redox cycles was observed. Thus, the data corresponding to the first cycle were used to determine the kinetics of fresh particles, whereas data corresponding to the fifth cycle were considered for the kinetics determination of "activated" particles.

To analyse the effect of the fuel gas concentration (CH_4, CO or H_2) on the reduction reaction rate four different concentrations are used: 5, 15, 30 and 60 vol.%. To determine the oxidation kinetics, oxygen concentrations of 5, 10, 15 or 21 vol.% were used. These oxidation experiments were carried out using 15 vol.% H_2 during the reduction step. All these experiments were carried out at 1073 K. To observe the effect

of temperature on the reaction rate, the reduction and oxidation reactions were carried out at the following temperatures: 973, 1023, 1073, 1123, 1173, 1223 and 1273 K. The fuel gas concentration during these experiments was 15 vol.%, whereas the oxygen concentration was 10 vol.%.

Besides, the oxygen release in nitrogen atmosphere was analysed at temperatures in the same temperature interval. In this case, the redox cycle consisted only of one oxidation period and one inert period in N_2.

3. Results

The oxygen transport capacity and reactivity with several reacting gases (CH_4, H_2, CO and O_2) as well as the oxygen uncoupling properties of the $CaMn_{0.775}Mg_{0.1}Ti_{0.125}O_{2.9-\delta}$ material were analysed in a TGA apparatus. In addition, the evolution of these properties with the cycle number was determined. From the evolution of solids conversion with time, at different operating conditions (temperature and gas concentration), the kinetics of reduction and oxidation reactions of the solid particles was obtained.

3.1. Oxygen transport capacity

The oxygen transport capacity of a perovskite type material, such as $CaMg_{0.1}Ti_{0.125}Mn_{0.775}O_{2.9-\delta}$, depends on the stoichiometric amount of oxygen in the oxidised and reduced material, i.e. the value of 2.9-δ. The general formula of the fully oxidized material is $CaMg_{0.1}Ti_{0.125}Mn_{0.775}O_{2.9}$, corresponding to the mixture $(CaO)_{0.225}\cdot(MgO)_{0.1}\cdot(TiO_2)_{0.125}\cdot(CaMnO_3)_{0.775}$. In presence of a reducing gas, e.g. CH_4, CO or H_2, $CaMnO_3$ can be reduced to $CaMnO_2$. This means that the reduced state is $CaMg_{0.1}Ti_{0.125}Mn_{0.775}O_{2.125}$, However, the oxygen uncoupling property is available while the perovskite structure is maintained. For example, reduction to $CaMnO_{2.81}$ could

be reached at 1273 K [33]. If more oxygen is removed from the solid crystal, the perovskite structure changes to the formation of $CaMn_2O_4$ or Ca_2MnO_4.

Taken H_2 as example, the oxygen transferred by the presence of a reducing gas corresponds to the following reaction:

$$CaMg_{0.1}Ti_{0.125}Mn_{0.775}O_{2.9} + 0.9\ H_2 \rightarrow CaMn_{0.9}Ti_{0.125}Mg_{0.1}O_2 + 0.9\ H_2O \quad (5)$$

The oxygen uncoupling reaction is considered only for the perovskite structure:

$$CaMg_{0.1}Ti_{0.125}Mn_{0.775}O_{2.9} \rightarrow CaMn_{0.9}Ti_{0.125}Mg_{0.1}O_{2.75} + 0.075\ O_2 \quad (6)$$

The mass difference between the oxidized and the reduced forms defines the oxygen transport capacity of the oxygen carrier, R_{OC}, which is calculated as:

$$R_{OC} = \frac{m_o - m_r}{m_o} \quad (7)$$

m_o and m_r being the masses of the oxidized and reduced forms of the material, respectively. Two different oxygen transport capacity definitions are used in this work:

(1) The total oxygen transport capacity, $R_{OC,t}$, describes the total fraction of oxygen which can be transferred to a fuel, e.g. CH_4, H_2 or CO corresponding to oxidized and reduced forms in Eq. (5). The total oxygen transport capacity of $CaMn_{0.775}Mg_{0.1}Ti_{0.125}O_{2.9-\delta}$ is $R_{OC,t}$ = 9.0 wt.%.

(2) The oxygen transport capacity for the oxygen uncoupling, $R_{OC,ou}$, describes the maximum oxygen available in solid for the oxygen uncoupling reaction; see Eq. (6). This reaction can happen without the presence of a reducing gas, and the maximum value for $R_{OC,ou}$ is 1.7 wt.%, corresponding to the oxygen loss given by Eq. (6).

Temperature programmed reduction (TPR) experiments were conducted in the TGA to determine the mass oxygen transport capacity of the perovskite material under nitrogen or reducing atmosphere. The oxidized state was considered to be fresh particles as

received after calcination in air. Thus, the mass loaded in the sample holder of the TGA was considered to be m_o as $CaMg_{0.1}Ti_{0.125}Mn_{0.775}O_{2.9}$.

Fig. 2 shows the normalized mass-loss variation, ω, during TPR experiments in N_2, H_2 or CH_4. The parameter ω represents the fraction of mass lost during reduction of fully oxidized oxygen carrier, and it was calculated as

$$\omega = \frac{m}{m_o} \tag{8}$$

The oxygen transport capacity can be calculated as

$$R_{OC} = 1 - \omega_r \tag{9}$$

ω_r being the normalized mass-loss when the sample was fully reduced.

When only N_2 was fed to the reactor, the oxygen generation started at a temperature of 1020 K and it slowly continued at the maximum temperature of 1273 K. In addition, the maximum normalized mass-loss variation corresponded to an oxygen transport capacity for the oxygen uncoupling property of $R_{OC,ou}$ = 1.4 wt.%. The oxygen released was slightly lower than that required to induce a change in the perovskite structure, which is 1.7 wt.%; see Eq. (6). After that, the reaction rate was slow due to the low driving force under this condition, i.e. the extremely low oxygen concentration at equilibrium conditions [27,33].

TPR tests were also carried out with 15 vol.% CH_4 or H_2; see Fig. 2. Here, the oxygen transport capacity in a reducing environment was determined. In both cases, the reaction started at 640 K. However, the reaction rate with H_2 was faster than with CH_4. In fact, reduction with H_2 was near finished when the reaction temperature was 1000 K, whereas reduction with CH_4 proceeds until temperature was 1250 K. Nevertheless, the normalized mass-loss of the fully reduced sample was the same in both cases (ω_r = 0.915). This fact indicates that the total oxygen transport capacity was the same

regardless of the reducing gas used. The oxygen transport capacity of the material to oxidize a fuel gas was $R_{OC,t}$ = 8.5 wt.%. This value is some lower than the correlated for the theoretical reduction from $CaMg_{0.1}Ti_{0.125}Mn_{0.775}O_{2.9}$ to $CaMg_{0.1}Ti_{0.125}Mn_{0.775}O_2$.

3.2. Evolution of the redox properties with the cycle number

Three series of ten reduction-oxidation cycles each series were carried out in the TGA at 1173 K to analyse the variation of oxygen transport capacity and reactivity of the oxygen carrier with the cycle number. Every cycle consisted of an inert period (300 s in N_2) followed by a reduction step with 15 vol.% CH_4 and oxidation by air. The time of reduction period was different in each series. Times of 20 s, 90 s, and 600 s were used. The oxidation period following the reduction with CH_4 lasted 180 s in all cases, assuring the maximum oxidation degree possible in every cycle.

3.2.1. Oxygen transport capacity

Figs. 3(a-c) show the normalized mass variation during each series of 10 cycles, with the only difference of the length of the reduction period. Obviously, the reduction period was longer, the reduction degree in every cycle was higher. In all cases, the oxygen carrier was not oxidized up to the same initial level. In fact, the degree of oxidation was decreasing with the cycle number, and it was more marked as the reduction period was increased. This fact indicates that the effective oxygen transport capacity decreases with the cycle number at these conditions. The initial oxygen transport capacity was $R_{OC,t}$ = 8.5 wt.%, but the final oxygen transport capacity was evaluated by the complete reduction of the sample after the 10^{th} redox cycle, being $R_{OC,t}$ = 8.0 wt.%.

Relevant is the fact that the oxygen uncoupling property of the $CaMg_{0.1}Ti_{0.125}Mn_{0.775}O_{2.9-\delta}$ material was maintained with the cycle number. The mass lost during 300 s in N_2 was about 0.8 wt.%, and it was maintained constant during the

redox cycles. The oxygen transport capacity could be affected by some formation of a compound with a lower oxidation state for manganese, e.g. $CaMn_2O_4$. Nevertheless, the intensity of $CaMn_2O_4$ formation would be low during consecutive redox cycles.

Some differences can be highlighted with respect the a previously tested material, i.e. $CaMg_{0.1}Mn_{0.9}O_{2.9-\delta}$ [27]. The oxygen transport capacity of $CaMg_{0.1}Mn_{0.9}O_{2.9-\delta}$ was higher ($R_{OC,t}$ = 10 wt.%), but it was decreased with the redox cycles during the activation period up to stabilise in $R_{OC,t}$ = 7.5 wt.%, which is lower than that for activated $CaMg_{0.1}Ti_{0.125}Mn_{0.775}O_{2.9}$. Also, the oxygen uncoupling property was mostly lost for $CaMg_{0.1}Mn_{0.9}O_{2.9-\delta}$, whereas the $CaMg_{0.1}Ti_{0.125}Mn_{0.775}O_{2.9-\delta}$ material maintains its oxygen uncoupling property, even when the oxygen carrier was highly reduced; see Fig. 3(c). Likely, the presence of Ti in the solid could stabilize the perovskite structure.

3.2.2. Reactivity

In any case, complete reduction with CH_4 was not reached during the first cycle, and a longer time than 600s would be required. But the reduction degree increased with the cycle number, indicating an activation process during consecutive redox cycles. The activation process happens even when the reduction period was very short (20 s), which is different than that found for $CaMg_{0.1}Mn_{0.9}O_{2.9-\delta}$, which maintained constant the reduction degree through the redox cycles when the reduction degree was low, i.e. activation was not found in this case. This fact agrees to results found during continuous operation, where $CaMg_{0.1}Mn_{0.9}O_{2.9-\delta}$ particles were not activated when the solids circulation was very high, i.e. the variation in solids conversion was low [22]. However, it can be advised that $CaMg_{0.1}Ti_{0.125}Mn_{0.775}O_{2.9-\delta}$ will be activated regardless the operating conditions in a CLC unit. In addition, the reactivity of $CaMg_{0.1}Ti_{0.125}Mn_{0.775}O_{2.9-\delta}$ with CH_4 at 1173 K is higher than that showed by $CaMg_{0.1}Mn_{0.9}O_{2.9-\delta}$.

The changes observed in reactivity were more intensive when the reduction was increased. This is a common finding with oxygen carrier materials prone to an activation process, e.g. a similar perovskite type material ($CaMn_{0.9}Mg_{0.1}O_{2.9-\delta}$) [22] or ilmenite [34]. However, there are not evidences for the ultimate reason of the reactivity increase in this case or other cases, but it was speculated that the increase of the porosity and/or a higher mobility of oxygen in the solid with the redox cycles could affect to the reactivity.

Thus, in the case of the longer reduction period (600 s) the reactivity increased up to the 2^{th}-3^{th} cycle and then stabilized. After that, complete reduction is reached in every cycle, see Fig. 3(c), and the time required for complete reduction was 150 s; but if reduction period was fixed to 150 s then more than 3 cycles would be necessary to get activation of particles due to the reduction degree affected to the velocity of the activation process. For example, 6-7 cycles was required to activate the material when the reduction period was lasted for 90 s; see Fig. 3(b).

Thus, it can be considered that the material has achieved a maximum conversion rate in reduction reaction from 3^{th} cycle. Similar redox cycles were carried out using H_2 or CO as reducing agent with reduction periods of 600 s, and similar results were found that those showed in Fig. 3(c).

In addition, the mass loss during the inert period was barely affected by the redox cycle, which suggests that the reactivity of the oxygen uncoupling mechanism was not affected by consecutives reduction and oxidation steps. This fact is a relevant issue, considering that a significant fraction of oxygen must be transferred to the fuel *via* oxygen uncoupling mechanism in order to get complete combustion with this kind of perovskite materials [15]. Again, $CaMg_{0.1}Ti_{0.125}Mn_{0.775}O_{2.9-\delta}$ improves the performance

of the $CaMg_{0.1}Mn_{0.9}O_{2.9-\delta}$ material, which lost most of oxygen uncoupling capacity after the activation process [27].

3.3. Kinetics determination for fresh and activated material

The reactivity and oxygen transport capacity of $CaMg_{0.1}Ti_{0.125}Mn_{0.775}O_{2.9-\delta}$ particles is different depending on the operating conditions and the number of redox cycles. Thus, the reaction rate of fresh and activated material is obtained under different temperatures (973-1273 K) and gas concentrations (5-60 vol.%). These results are presented as conversion vs. time curves and are used to determine the kinetic parameters of the reduction and oxidation reactions.

The conversion values are obtained from the following equations:

$$X_r = \frac{m_o - m}{R_{OC} m_o} \tag{10}$$

$$X_o = \frac{m - m_r}{R_{OC} m_o} \tag{11}$$

for the reduction and oxidation reaction, respectively. The oxygen transport capacity corresponding to the reaction considered and reacting temperature must be used. When reduction by a fuel gas is considered, $R_{OC,t}$ averaged a value of 8.5 wt.% for fresh material, whereas for activated particles the $R_{OC,t}$ value is 8.0 wt.%. For the oxygen uncoupling reaction, the $R_{OC,ou}$ value was 1.4 wt.%. Conversion values ranged from 0 to 1 in all cases.

3.3.1. Effect of fuel type

Common reducing gases during fuel combustion in a CLC system are CH_4, H_2 and CO. So, the reactivity with these gases was evaluated. To compare the oxygen carrier reactivity with these gases, Figs. 4 show the conversion vs. time curves for the different reducing gases. Conversion vs. time curves for activated material was taken from the 5^{th} redox cycle. The reactivity followed the order $H_2 > CO > CH_4$ for fresh particles,

whereas it was H_2 > CH_4 > CO for activated particles. It is necessary to activate the particles to found a high reactivity with methane. During the activation process, the reactivity increased by 2 with CH_4, by 1.5 with H_2 and by 1.2 with CO. However, reactivity for oxidation reaction was unchanged. Moreover, the oxidation rate was not dependent on the fuel gas used in the previous reduction stage.

Nevertheless, the oxygen transport capacity was decreased during activation. Thus, a value of $R_{OC,t}$ = 8.5 wt.% was taken for fresh particles and $R_{OC,t}$ = 8.0 wt.% for activated particles. This decrease was due to the oxygen carrier was not able to recover the initial oxidation state.

Moreover, the conversion vs. time curves obtained in pure N_2 are also showed in Figs. 4 for fresh and activated material. No major differences are found between oxygen uncoupling reactivity of fresh and activated particles. It was found that the reaction rate of the oxygen uncoupling mechanism is lower than the reduction rate by 15 vol.% of any fuel gas. However, the oxygen uncoupling mechanism could be relevant when the fuel concentration around particles was low in the fuel reactor.

3.3.2. Effect of gas concentration

To determine the effect of the gas concentration on the kinetics of the reduction reaction, several experiments at 1073 K with different gas concentrations were carried out. The conversion vs. time curves obtained with CH_4, H_2, CO or O_2 as reacting gases are shown in Figs. 5 and 6 for fresh and activated particles, respectively. There was a direct relationship between the fuel concentration and the reaction rate. As expected, an increase in the fuel gas concentration produced an increase in the reaction rate.

3.3.3. Effect of reacting temperature

The effect of temperature on the reaction rate was investigated in the interval 973-1273 K. Figs. 7(a-d) show the conversion vs. time curves for the reduction of fresh material with CH_4, H_2 and CO, as well as the oxidation with O_2. Similarly, Figs. 8(a-d) show the conversion vs. time curves for activated particles. In all cases, the reaction rate was affected by the temperature. An increase of temperature produced an increase in the reduction rate, although this effect was rather low for oxidation.

It was observed a decrease of the reaction rate with the conversion of solids, especially for fresh particles and reaction with CH_4 or CO at low temperature. This fact can indicate a change in the controlling mechanism of the reaction, likely from a chemical reaction control to a control by the diffusion in the product layer of the grains at high conversion values. The decrease of the reaction rate with conversion was less relevant at high temperatures ($\geq$ 1223 K) or for activated material, suggesting that the diffusion in the product layer had lower importance at these conditions. To predict the experimental results, both chemical reaction and diffusion in the product layer should be taken into account when the kinetic model was formulated.

The effect of temperature on the oxygen uncoupling rate of fresh and activated particles was also analysed. Fig. 9 shows the conversion vs. time curves obtained during reaction in pure N_2. It can be observed the necessity of high temperatures to reach high oxygen uncoupling reaction rates. Also it is highlighted that the oxygen uncoupling rate is higher for activated particles at low temperature, whereas it is the contrary at high temperatures.

4. Kinetic model

The grain model was considered for reduction and oxidation reactions. The particle was assumed to be formed by a certain amount of spherical grains, each following the shrinking core model (SCM) during reduction or oxidation [35]. Some information on the controlling mechanism can be extracted from the shape of the conversion vs. time curves. It was observed that reduction with a fuel gas or oxidation by oxygen showed a linear dependence with the reacting time at low conversion values, and the reaction rate decreased with time at higher conversion of solids. In fact, there was a sharp decrease of the reaction rate in some cases. The linear dependence of conversion with time can be attributed to reaction in the gas-solid interphase with chemical reaction control onto the gas-solid interphase. Besides, the decrease of the reaction rate at higher conversion values was attributed to a change in the controlling mechanism from chemical reaction to diffusion through the product layer around the grains.

With all above considerations, and considering negligible the resistances to gas film mass transfer and the diffusion inside the particle, the equations that describe this model are the following [36]:

$$t = \tau_{ch} X + \tau_{pl}\left(1 - 3\left(1 - X\right)^{2/3} + 2\left(1 - X\right)\right) \tag{12}$$

where

$$\tau_{ch} = \frac{1}{k_s C_i^n} \tag{13}$$

$$k_s = k_{s,0} \mathrm{e}^{-E_{ch}/R_g T} \tag{14}$$

and

$$\tau_{pl} = \frac{1}{D_{pl} C_i^{n'}} \tag{15}$$

$$D_{pl} = D_{pl,0} \mathrm{e}^{E_{pl}/R_g T - k_X X} \quad (16)$$

In this case, the parameter k_X is included to consider the sharp decrease in the reaction rate with time.

In the case of the oxygen uncoupling reaction, the oxygen concentration at equilibrium was considered. Only chemical reaction control was considered, and the evolution of conversion with time was defined by the following equation:

$$t = \frac{1}{k_s \left(C_{O_2,eq}^n - C_{O_2}^n\right)} X \quad (17)$$

The oxygen concentration at equilibrium conditions depends on temperature and sharply decreases with solids conversion, and it was calculated as previously reported [27].

5. Determination of kinetic parameters

5.1. Reduction and oxidation reactions

The kinetic model described in Section 4 was used to determine the kinetic parameters for the reduction reaction with CH_4, H_2 and CO and oxidation with O_2. The kinetic parameters of the chemical reaction for the reactions considered were obtained from an analysis of τ_{ch} values obtained for different gas concentrations and temperatures. Figs. 10(a) and (b) show a plot of $\ln(1/\tau_{ch})$ vs. $\ln(C_i)$ for reaction with CH_4, H_2, CO or O_2 for fresh and activated particles, respectively. The reaction order, n, was obtained from the slope of the figure, being $\ln(k_s)$ the intercept. The chemical reaction kinetic constant, k_s, as a function of the temperature was obtained from experiments carried out at different temperatures.

Figs. 11(a) and (b) show the Arrhenius plot of ln(k_s) values as a function of 1/T for fresh and activated particles. The slope of the curves is E_{ch}/R_g, whereas the intercept value is ln($k_{s,0}$). The calculated kinetic parameters for each reaction are shown in Tables 1 and 2. Once the kinetic parameters for chemical reaction were obtained, the kinetic parameters for diffusion through the product layer were obtained by fitting the conversion curves obtained at different gas concentrations and temperatures. It was found that the diffusion mechanism was dependent on the reacting gas concentration in both reduction and oxidation reactions. The value of the exponent n' ranged between 0.7 and 1. This result suggests that the main limiting process was the diffusion of reacting compounds throughout the product layer, which agrees with the formulation of the kinetic model. Values of the initial effective diffusivity in the product layer, D_{pl}, (i.e. for X = 0) were obtained at each temperature in order to fit the conversion vs. time curves. The value of D_{pl} decreased as the solids conversion increased by the use of the decay constant, k_X; see Eq. (16). A constant value for k_X with temperature was obtained for every reaction. To obtain the activation energy of the diffusion in the product layer, E_{pl}, the values of D_{pl} at zero conversion were used. Thus, assuming the Arrhenius dependence for D_{pl} with the temperature, the values of the corresponding pre-exponential factor, and the activation energies were obtained from Figs. 12(a) and (b) and they are showed in Tables 1 and 2 for fresh and activated solid.

5.2. Oxygen uncoupling reaction

In this case, a τ_{ch} value was not adequate to describe the reaction progress because the oxygen concentration at equilibrium conditions changes with the solids conversion. So, a value of k_s was determined for every temperature by fitting experimental conversion vs. time curves by Eq. (17). The reaction order affected to the curvature of the conversion vs. time lines. So, reaction order was also determined by the fitting method

of lines. The dependence of k_s values with temperature for the oxygen uncoupling reaction is shown for fresh and activated material in Figs. 11(a) and (b), and the kinetic parameters are shown in Tables 1 and 2. It is interesting to note the negative value for the activation energy for activated particles. From conversion vs. time curves in Figs. 9(a) and (b) is evident that the activation energy for fresh particles must be higher than for activated particles. But a negative value for the activation energy has not sense. The problem can be related to the assumption that determination of oxygen concentration at equilibrium conditions for activated material is equal than for fresh particles. An erroneous calculation of the oxygen concentration at equilibrium in Eq. (17) can give an unexpected variation of k_s with temperature. Future work to determine thermodynamic properties of fresh and activated $CaMg_{0.1}Ti_{0.125}Mn_{0.775}O_{2.9-\delta}$ material should be done in order to confirm this hypothesis and to find adequate values for the equilibrium concentration of the activated material. Nevertheless, the reaction model with kinetic parameters calculated in this work can be used with confidence in a reactor model in the temperature interval considered in this work, i.e. 973-1273 K.

The conversion vs time curves predicted by the reaction model with the kinetic parameters obtained are shown in Figs. 5-9. As it can be seen, the conversion curves are well predicted in all range of operating conditions studied, i.e. gas concentration, temperature or reaction type.

6. Evaluation of oxygen carrier reactivity

To evaluate the oxygen carrier reactivity, as a basis for comparison with other oxygen carrier materials, a method previously proposed is used [37]. So, the minimum solids inventory in fuel or air reactor is calculated using kinetics determined in this work with the following equations:

$$m_{FR,\min} = \frac{2\ d\ M_O}{R_{OC}\ \Delta H_c^0} \frac{1}{\left[dX_r/dt\right]_{X_r \to 0}} \tag{18}$$

$$m_{AR,\min} = \frac{2\ d\ M_O}{R_{OC}\ \Delta H_c^0} \frac{1}{\left[dX_o/dt\right]_{X_o \to 0}} \tag{19}$$

Note that the oxygen transport capacity with a fuel gas $R_{OC,t}$, was higher than the oxygen transport capacity for oxygen uncoupling reaction, $R_{OC,ou}$.

The minimum oxygen carrier inventory in the fuel and air reactor is a suitable parameter to compare the performance of a material as oxygen carrier regarding the fuel combustion and regeneration in fuel and air reactors, respectively. Ideally, the minimum solids inventory is calculated for values of $\Delta X \to 0$, where the reaction is only controlled by chemical reaction. Thus, the chemical reaction control was assumed to be the controlling mechanism to calculate the reaction rates. Moreover, the reaction rates were calculated for an average gas concentration calculated by:

$$\bar{C}_i = \frac{\Delta X_g \cdot C_{i,0}^n}{\int_{Xg,in}^{Xg,out} \left[\frac{1+\varepsilon_g \cdot X_g}{1-X_g}\right]^n dX_g} \tag{20}$$

ε_g represents the expansion of volume as a result of the chemical reaction and it takes values of 2 for CH_4, 0 for CO and H_2, and -0.21 for oxygen in air [37]. The calculated average gas concentration for a fuel conversion of 99.9% depends on the reaction order, being: 19.2 vol.% for H_2 and CO or 11.1 vol.% O_2 in all cases; and 5.3 vol.% CH_4 or 13.3 vol.% CH_4 for fresh and activated particles, respectively. In the case of the oxygen uncoupling rate, it was an average oxygen concentration in order to maximize the reaction rate; the oxygen concentration at equilibrium was given by the maximum oxidation state in the air reactor, i.e. it was assumed 4 vol.% O_2 [27].

Figure 13 shows the minimum solids inventory in the fuel and air reactor for fresh and activated particles. The values obtained for the $CaMg_{0.1}Mn_{0.9}O_{2.9-\delta}$ material previously tested is also included for comparison purposes. The solids inventory values for perovskite materials are values are lower than calculated for other Mn-based materials [3,38]. In general, solids inventory for $CaMg_{0.1}Ti_{0.125}Mn_{0.775}O_{2.9-\delta}$ is lower than for $CaMg_{0.1}Mn_{0.9}O_{2.9-\delta}$ when H_2 or CO is considered the fuel, as well as for the oxygen uncoupling reaction is relevant; the opposite is observed for CH_4 combustion and oxidation in the air reactor. It is relevant the fact that the $CaMg_{0.1}Ti_{0.125}Mn_{0.775}O_{2.9-\delta}$ material retains the oxygen uncoupling property in activated particles, which was lost in $CaMg_{0.1}Mn_{0.9}O_{2.9-\delta}$ [27]. Also, the addition of Ti to the perovskite improved the reactivity for oxygen uncoupling.

Solids inventory follows the reactivity order with different gases, i.e. more reactive is the gas, lower inventory is required. Also, fresh particles required a higher amount of solids in the fuel reactor than activated particles owing to the lower reactivity of fresh particles; however the solids inventory in the air reactor was roughly the same for fresh and activated particle because oxidation rate was unaffected by redox cycles.

For the oxygen uncoupling mechanism, the calculated amount of solids in the fuel reactor was higher than those calculated for the gas-solid reaction between fuel and oxygen carrier, mainly due to $R_{OC,ou} < R_{OC,t}$. Nevertheless, it was determined that oxygen uncoupling can be relevant to get complete combustion of methane with $CaMnO_{3-\delta}$-based materials [15]. In this way, the solids inventory values in the fuel reactor calculated for CH_4, H_2 and CO were equal to those given for oxygen uncoupling in Table 3 when the fuel gas concentration was 1.2 vol.% CH_4, 0.38 vol.% H_2, or 0.85 vol.% CO for fresh particles; and 0.01 vol.% CH_4, 0.38 vol.% H_2, or 1 vol.% CO for activated particles. This suggest that the oxygen uncoupling mechanism would be

relevant in order to fully convert the fuel gas in the upper part of the fluidized bed reactor, i.e. when the fuel gas concentration is low. Note that the oxygen transferred via oxygen uncoupling is less prone to diffusional restrictions than gas-solid reactions, which makes the oxygen uncoupling a good complement to gas-solid reactions during fuel conversion in the fuel reactor [8,10,15].

7. Conclusions

The oxygen transport capacity and reactivity of $CaMg_{0.1}Ti_{0.125}Mn_{0.775}O_{2.9-\delta}$ material for the reduction and oxidation reactions were determined by thermogravimetric analysis using CH_4, H_2, CO or O_2 as reacting gases. Besides, the oxygen uncoupling property of this material was analysed. These reactions correspond to processes happening in Chemical Looping Combustion (CLC) and Chemical Looping with Oxygen Uncoupling (CLOU) processes.

This material showed an activation process for reduction reaction with the redox cycles. During the activation process the reactivity with fuel gases was increased. Moreover, the oxygen transport capacity decreased from $R_{OC,t}$ = 8.5 wt.% to $R_{OC,t}$ = 8.0 wt.%. Nevertheless, the oxygen uncoupling property was maintained during redox cycles, with an oxygen loss of 1.4 wt.% at 1273 K in N_2. The oxidation reactivity was not affected by the cycle number.

The grain model, assuming mixed control by the chemical reaction and the diffusion through the product layer, was able to predict the experimental results under different gas concentration, temperature or reaction type. Reaction kinetic for reduction, oxidation and oxygen uncoupling process for fresh and activated particles were determined. The kinetic data obtained in this work will be useful to be included in mathematical models of CLC reactors with $CaMg_{0.1}Ti_{0.125}Mn_{0.775}O_{2.9-\delta}$ material as

oxygen carrier. The choice of the kinetic parameters must be suited to the characteristics of the particles used, i.e. fresh or activated particles. Moreover, oxygen uncoupling process can be relevant and this mechanism should be considered in fuel reactor modelling.

Acknowledgments

This paper is based on the work produced within the framework of the INNOCUOUS (Innovative Oxygen Carriers Uplifting Chemical Looping Combustion) Project, funded by the European Commission under the Seventh Framework Programme (Contract 241401). The authors thank Frans Snijkers from VITO and Prof. Anders Lyngfelt from Chalmers University of Technology for supplying the $CaMg_{0.1}Ti_{0.125}Mn_{0.775}O_{2.9-\delta}$ material.

Submitted, accepted and published by
Chemical Engineering Journal 2015, 269, 67-81

8. Nomenclature

C_i = reacting concentration of gas *i* (mol/m^3)

D_{pl} = effective product layer diffusivity (m^{3n} mol^{-n} s^{-1})

$D_{pl,0}$ = pre-exponential factor for effective product layer diffusivity (m^{3n} mol^{-n} s^{-1})

E_i = activation energy of the process *i* (J/mol)

k_s = chemical kinetic constant (m^{3n} mol^{-n} s^{-1})

$k_{s,0}$ = pre-exponential factor for chemical kinetic constant (m^{3n} mol^{-n} s^{-1})

k_X = decay constant for the product layer diffusivity

m = instantaneous mass of oxygen carrier (kg)

m_o = mass of the oxidized form of the oxygen carrier (kg)

m_r = mass of the reduced form of the oxygen carrier (kg)

n = reaction order for chemical reaction

n' = exponential constant for gas concentration in the product layer diffusion process

R_g = constant for ideal gases (R_g = 8.314 J mol^{-1} K^{-1})

R_{OC} = oxygen transport capacity

$R_{OC,ou}$ = oxygen transport capacity for oxygen uncoupling process

$R_{OC,t}$ = total oxygen transport capacity with a fuel gas

t = time (s)

T = temperature (K)

X = conversion of solids

Greek symbols

γ = parameter in subscript for oxygen in the reduced state

δ = parameter in subscript for oxygen in the oxidized state

τ_i = time for complete conversion when the reaction is controlled by the process *i* (s)

ω = normalized mass-loss variation

Subscripts

ch = chemical reaction

eq = equilibrium

o = oxidation

ou = oxygen uncoupling

pl = product layer

r = reduction

9. References

[1] IPCC, 2005. Special report on carbon dioxide capture and storage. Working group II of the Intergovernmental Panel on Climate Change, Editors: B. Metz, O. Davidson, H. de Coninck, M. Loos, L. Meyer, Cambridge University Press, Cambridge, UK and New York, NY, USA, 2005.

[2] L.I. Eide, M. Anheden, A. Lyngfelt, C. Abanades, M. Younes, D. Clodic, Novel Capture Processes, Oil Gas Sci. Technol. 60 (2005) 497-508.

[3] J. Adanez, A. Abad, F. Garcia-Labiano, P. Gayan, L.F. de Diego, Progress in Chemical-Looping Combustion and Reforming technologies, Prog. En. Comb. Sci. 38 (2012) 215-282.

[4] T. Mattisson, A. Lyngfelt, H. Leion, Chemical-looping with oxygen uncoupling for combustion of solid fuels, Int. J. Greenhouse Gas Control 3 (2009) 11-19.

[5] T. Mattisson, Materials for Chemical-Looping with Oxygen Uncoupling, ISRN Chemical Engineering 2013 (2013) Article ID 526375.

[6] Q. Imtiaz, D. Hosseini, C.R. Müller, Review of Oxygen Carriers for Chemical Looping with Oxygen Uncoupling (CLOU): Thermodynamics, Material Development, and Synthesis, Energy Technol. 1 (2013) 633-647.

[7] M. Rydén, H. Leion, T. Mattisson, A. Lyngfelt, Combined oxides as oxygen carrier material for chemical looping with oxygen uncoupling, Proc. 2nd Int. Conf. Chemical Looping, Darmstadt, Germany (2012).

[8] A. Abad, I. Adánez-Rubio, P. Gayán, F. García-Labiano, L.F. de Diego, J. Adánez, Demonstration of chemical-looping with oxygen uncoupling (CLOU) process in a 1.5 kW_{th} continuously operating unit using a Cu-based oxygen-carrier, Int. J. Greenhouse Gas Control 6 (2012) 189-200.

[9] I. Adánez-Rubio, A. Abad, P. Gayán, L.F. de Diego, F. García-Labiano, J. Adánez, Performance of CLOU process in the combustion of different types of coal with CO_2 capture, Int. J. Greenhouse Gas Control 12 (2013) 430-440.

[10] I. Adánez-Rubio, A. Abad, P. Gayán, L.F. de Diego, F. García-Labiano, J. Adánez, Biomass combustion with CO_2 capture by chemical looping with oxygen uncoupling (CLOU), Fuel Proc. Tech. 124 (2014) 104-114.

[11] I. Adánez-Rubio, A. Abad, P. Gayán, F. García-Labiano, L.F. de Diego, J. Adánez, The fate of sulphur in the Cu-based Chemical Looping with Oxygen Uncoupling (CLOU) Process, Applied Energy 113 (2014) 1855-1862.

[12] A. Shulman, E. Cleverstam, T. Mattisson, A. Lyngfelt, Chemical-Looping with oxygen uncoupling using Mn/Mg-based oxygen carriers – Oxygen release and reactivity with methane, Fuel 90 (2011) 941-950.

[13] I. Adánez-Rubio, A. Abad, P. Gayán, L.F. de Diego, F. García-Labiano, J. Adánez, Identification of operational regions in the Chemical-Looping with Oxygen Uncoupling (CLOU) process with a Cu-based oxygen carrier, Fuel 102 (2012) 634-645.

[14] D. Mei, A. Abad, H. Zhao, J. Adánez, Characterization of a Sol-gel Derived $CuO/CuAl_2O_4$ Oxygen Carrier for Chemical Looping Combustion (CLC) and Chemical Looping with Oxygen Uncoupling (CLOU) of Gaseous Fuels, Submitted for publication (2014).

[15] A. Abad, P. Gayán, L.F. de Diego, F. García-Labiano, J. Adánez, K. Mayer, S. Penthor, Modelling a CLC process improved by CLOU and validation in a 120 kW unit, Proc. 11th Int. Conf. Fluidized Bed Technology (CFB-11), Beijing, China (2014).

[16] J.E. Readman, A. Olafsen, Y. Larring, R. Blom, $La_{0.8}Sr_{0.2}Co_{0.2}Fe_{0.8}O_{3-\delta}$ as a potential oxygen carrier in a chemical looping type reactor, an in-situ powder X-ray diffraction study, J. Mater. Chem. 15 (2005) 1931-1937.

[17] M. Rydén, A. Lyngfelt, T. Mattisson, D. Chen, A. Holmen, E. Bjørgum, Novel oxygen-carrier materials for chemical-looping combustion and chemical-looping reforming; $La_xSr_{1-x}Fe_yCo_{1-y}O_{3-\delta}$ perovskites and mixed-metal oxides of NiO, Fe_2O_3 and Mn_3O_4, Int. J. Greenhouse Gas Control 2 (2008) 21-36.

[18] A. Fossdal, E. Bakken, B.A. Øye, C. Schøning, I. Kaus, T. Mokkelbost, Y. Larring, Study of inexpensive oxygen carriers for chemical looping combustion, Int. J. Greenhouse Gas Control 5 (2011) 483-488.

[19] H. Leion, Y. Larring, E. Bakken, R. Bredesen, T. Mattisson, A. Lyngfelt, Use of $CaMn_{0.875}Ti_{0.125}O_3$ as Oxygen Carrier in Chemical-Looping with Oxygen Uncoupling, Energy Fuels 23 (2009) 5276-5283.

[20] M. Rydén, A. Lyngfelt, T. Mattisson, $CaMn_{0.875}Ti_{0.125}O_3$ as oxygen carrier for chemical-looping combustion with oxygen uncoupling (CLOU) - Experiments in a continuously operating fluidized-bed reactor system, Int. J. Greenhouse Gas Control 5 (2011) 356-366.

[21] P. Hallberg, D. Jing, M. Rydén, T. Mattisson, A. Lyngfelt, Chemical Looping Combustion and Chemical Looping with Oxygen Uncoupling Experiments in a Batch Reactor Using Spray-Dried $CaMn_{1-x}M_xO_{3-\delta}$ (M = Ti, Fe, Mg) Particles as Oxygen Carriers, Energy Fuels 27 (2013), 1473-1481.

[22] A. Cabello, A. Abad, P. Gayán, L.F. de Diego, F. García-Labiano, J. Adánez, Effect of Operating Conditions and H_2S Presence on the Performance of $CaMg_{0.1}Mn_{0.9}O_{3-\delta}$ Perovskite Material in Chemical Looping Combustion (CLC), Energy Fuels 28 (2014) 1262-1274.

[23] M. Källén, M. Rydén, C. Dueso, T. Mattisson, A. Lyngfelt, $CaMn_{0.9}Mg_{0.1}O_{3-\delta}$ as Oxygen Carrier in a Gas-Fired 10 kW_{th} Chemical-Looping Combustion Unit, Ind. Eng. Chem. Res. 52 (2013) 6923-6932.

[24] K. Mayer, T. Pröll, H. Hofbauer, Pilot plant testing of Fe- and Mn-based oxygen carriers for chemical looping combustion, 5th High Temperature Solid Looping Network Meeting, Cambridge, UK (2013).

[25] C. Linderholm, A. Abad, T. Mattisson, A. Lyngfelt, 160 h of chemical-looping combustion in a 10 kW reactor system with a NiO-based oxygen carrier, Int. J. Greenhouse Gas Control 2 (2008) 520-530.

[26] P. Kolbitsch, J. Bolhàr-Nordenkampf, T. Pröll, H. Hofbauer, Comparison of Two Ni-Based Oxygen Carriers for Chemical Looping Combustion of Natural Gas in 140 kW Continuous Looping Operation, Ind. Eng. Chem. Res. 48 (2009) 5542-5547.

[27] L.F. de Diego, A. Abad, A. Cabello, P. Gayán, F. García-Labiano, J. Adánez, Reduction and Oxidation Kinetics of a $CaMn_{0.9}Mg_{0.1}O_{3-\delta}$ Oxygen Carrier for Chemical-Looping Combustion, Ind. Eng. Chem. Res. 53 (2014) 87-103.

[28] F. Snijkers, D. Jing, J. van Noyen, T. Mattisson, M. Jacobs, A. Lyngfelt, Preparation and properties of perovskite Mn-based oxygen carriers for Chemical Looping Combustion by industrial spray drying method, Proc. 3rd Int. Conf. Chemical Looping, Göteborg, Sweden (2014).

[29] P. Hallberg, M. Källén, D. Jing, F. Snijkers, J. van Noyen, M. Rydén, A. Lyngfelt, Experimental Investigation of $CaMnO_{3-\delta}$ Based Oxygen Carriers Used in Continuous Chemical-Looping Combustion, International Journal of Chemical Engineering 2014 (2014) Article ID 412517.

[30] C. Dueso, M. Ortiz, A. Abad, F. García-Labiano, L.F. de Diego, P. Gayán, J. Adánez, Reduction and oxidation kinetics of nickel-based oxygen-carriers for chemical-looping combustion and chemical-looping reforming, Chem. Eng. J. 188 (2012) 142-154.

[31] A. Cabello, A. Abad, F. García-Labiano, P. Gayán, L.F. de Diego, J. Adánez, Kinetic determination of a highly reactive impregnated Fe_2O_3/Al_2O_3 oxygen carrier for use in gas-fueled Chemical Looping Combustion, Chem. Eng. J. 258 (2014) 265-280.

[32] I. Adanez-Rubio, P. Gayan, A. Abad, F. Garcia-Labiano, L.F. de Diego, J. Adanez, Kinetic analysis of a Cu-based oxygen carrier: Relevance of temperature and oxygen partial pressure on reduction and oxidation reactions rates in Chemical Looping with Oxygen Uncoupling (CLOU), Chem. Eng. J. 256 (2014) 69-84.

[33] E.I. Leonidova, I.A. Leonidov, M.V. Patrakeev, V.L. Kozhevnikov, Oxygen non-stoichiometry, high-temperature properties, and phase diagram of $CaMnO_{3-\delta}$, J. Solid State Electrochem. 15 (2011) 1071-1075.

[34] J. Adánez, A. Cuadrat, A. Abad, P. Gayán, L.F. de Diego, F. García-Labiano, Ilmenite Activation during Consecutive Redox Cycles in Chemical-Looping Combustion, Energy Fuels 24 (2010) 1402-1413.

[35] J. Szekely, J.W. Evans, A structural model for gas-solid reactions with a moving boundary, Chem. Eng. Sci. 25 (1970) 1091.

[36] O. Levenspiel, Chemical Reaction Engineering; John Wiley and Sons: New York, 1981.

[37] A. Abad, J. Adánez, F. García-Labiano, L.F. de Diego, P. Gayán, J. Celaya, Mapping of the range of operational conditions for Cu-, Fe-, and Ni-based oxygen carriers in chemical-looping combustion, Chem. Eng. Sci. 62 (2007) 533-549.

[38] Q. Zafar, A. Abad, T. Mattisson, B. Gevert, M. Strand, Reduction and oxidation kinetics of Mn_3O_4/Mg-ZrO_2 oxygen carrier particles for chemical-looping combustion, Chem. Eng. Sci. 62 (2007) 6556.

Submitted, accepted and published by
Chemical Engineering Journal 2015, 269, 67-81

Figure captions

Fig. 1. Reactor scheme of the CLC process.

Fig. 2. Normalized mass-loss profiles for TPR (20 K/min) in TGA in (————) 100 vol.% high purity N_2, (– – – – –) 15 vol.% CH_4 and (— — —) 15 vol.% H_2, as well as temperature evolution (— · — · —).

Fig. 3. Normalized mass variations during reduction-oxidation cycles in TGA starting from fresh particles. Reduction environment:100 vol.% N_2 for 300 s, followed by reduction with 15 vol.% CH_4 + 20 vol.% H_2O, and oxidation by air for 180 s. The reduction period with CH_4 in each figure was (a) 20 s, (b) 90 s and (c) 600 s. T=1173 K.

Fig. 4. Conversion vs. time curves during reduction period with CH_4, H_2 or CO and oxidation period by O_2 for (a) fresh particles and (b) activated particles. T = 1173 K; fuel: 15 vol.%; O_2: 10 vol.%.

Fig. 5. Effect of gas concentration on the reaction rate of fresh particles with (a) CH_4; (b) H_2; (c) CO; and (d) O_2. T = 1073 K. Symbols: experimental curve. Continuous line: model predictions.

Fig. 6. Effect of gas concentration on the reaction rate of activated particles with (a) CH_4; (b) H_2; (c) CO; and (d) O_2. T = 1073 K. Symbols: experimental curve. Continuous line: model predictions.

Fig. 7. Effect of temperature on the reaction rate of fresh particles with (a) CH_4; (b) H_2; (c) CO; and (d) O_2. 15 vol.% reducing agent or 10 vol.% O_2. Symbols: experimental curve. Continuous line: model predictions.

Fig. 8. Effect of temperature on the reaction rate of activated particles with (a) CH_4; (b) H_2; (c) CO; and (d) O_2. 15 vol.% reducing agent or 10 vol.% O_2. Symbols: experimental curve. Continuous line: model predictions.

Fig. 9. Effect of temperature on the oxygen uncoupling reaction rate of (a) fresh and (b) activated particles in pure N_2. Symbols: experimental curve. Continuous line: model predictions.

Fig. 10. Plot to obtain the reaction order with respect to CH_4, H_2, CO and O_2 for (a) fresh and (b) activated particles. T = 1073 K.

Fig. 11. Arrhenius plot for the kinetic constant k_s for the reaction of CH_4, H_2, CO and O_2 for (a) fresh and (b) activated particles. The kinetic constant values for oxygen uncoupling reaction in N_2 for fresh particles are also included.

Fig. 12. Arrhenius plot for the effective diffusivity in the product layer D_{pl} for the reaction of CH_4, H_2, CO and O_2 for (a) fresh and (b) activated particles.

Fig. 13. Minimum solids inventory in the fuel and air reactors for $CaMg_{0.1}Ti_{0.125}Mn_{0.775}O_{2.9-\delta}$ following the method proposed in [37]. Values obtained for $CaMg_{0.1}Mn_{0.9}O_{2.9-\delta}$ are also presented for comparison purposes [27].

Submitted, accepted and published by
Chemical Engineering Journal 2015, 269, 67-81

Table captions

Table 1. Kinetic parameters for reaction of fresh $CaMg_{0.1}Ti_{0.125}Mn_{0.775}O_{2.9-\delta}$ particles with CH_4, CO, H_2 and O_2, and oxygen uncoupling in N_2.

Table 2. Kinetic parameters for reaction of activated $CaMg_{0.1}Ti_{0.125}Mn_{0.775}O_{2.9-\delta}$ particles with CH_4, CO, H_2 and O_2, and oxygen uncoupling in N_2.

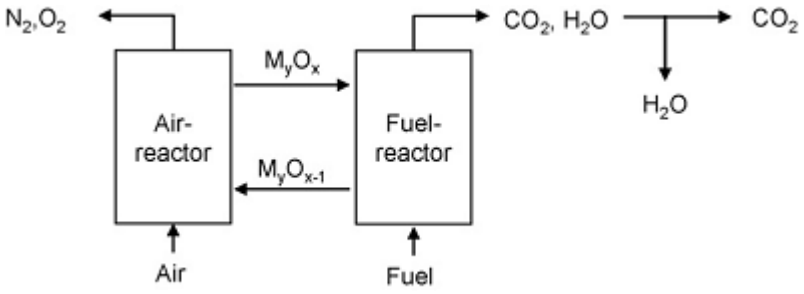

Fig. 1. Reactor scheme of the CLC process.

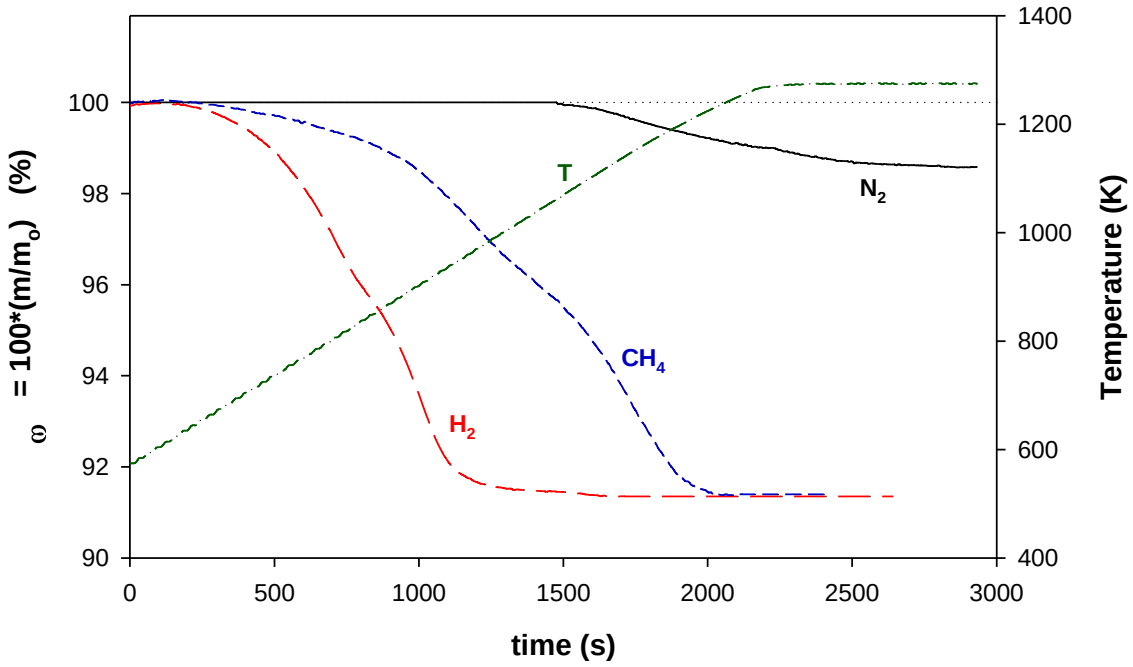

Fig. 2. Normalized mass-loss profiles for TPR (20 K/min) in TGA in (————) 100 vol.% high purity N_2, (– – – – –) 15 vol.% CH_4 and (— — —) 15 vol.% H_2, as well as temperature evolution (—·—·—).

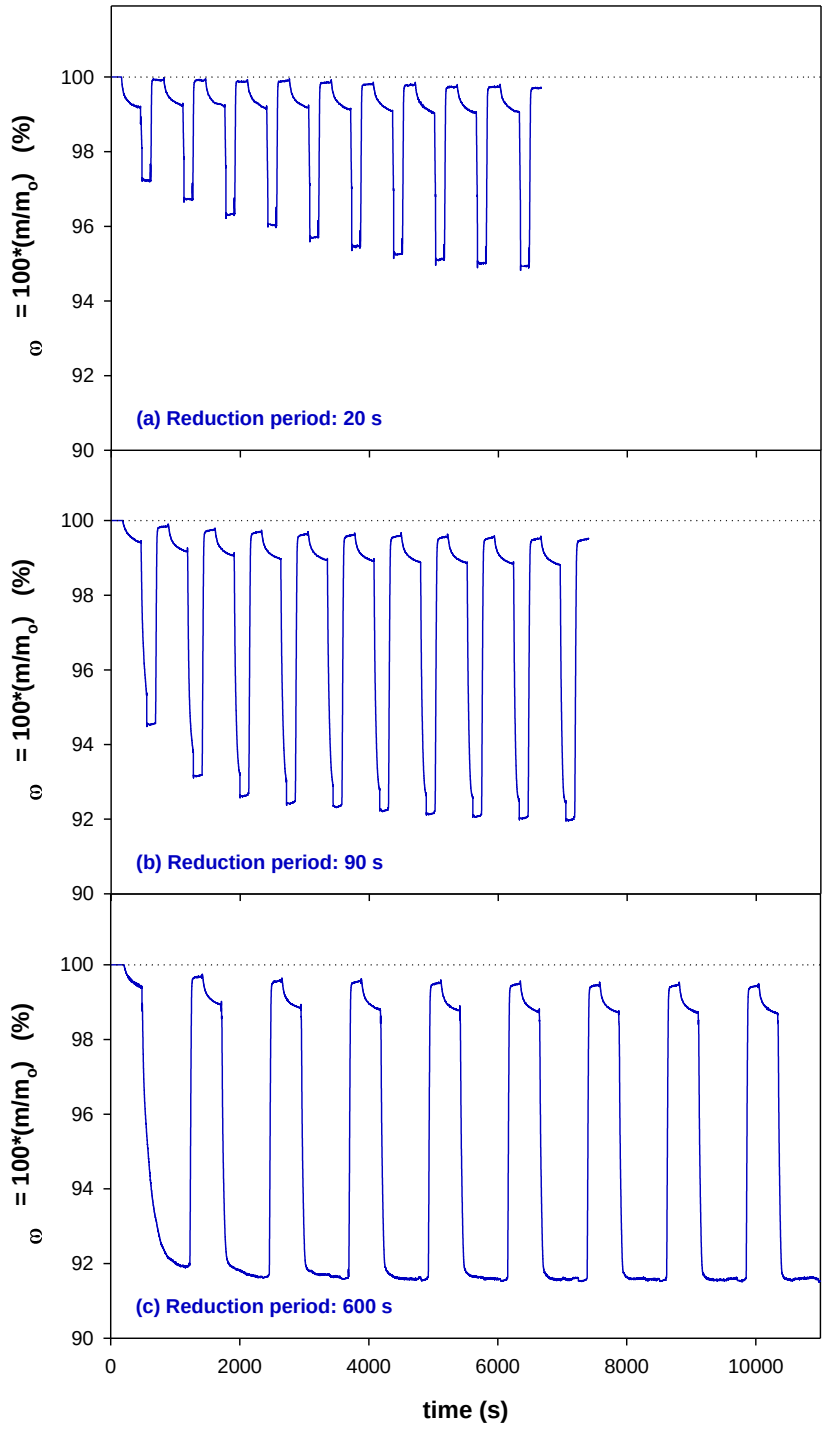

Fig. 3. Normalized mass variations during reduction-oxidation cycles in TGA starting from fresh particles. Reduction environment:100 vol.% N_2 for 300 s, followed by reduction with 15 vol.% CH_4 + 20 vol.% H_2O, and oxidation by air for 180 s. The reduction period with CH_4 in each figure was (a) 20 s, (b) 90 s and (c) 600 s. T=1173 K.

Submitted, accepted and published by
Chemical Engineering Journal 2015, 269, 67-81

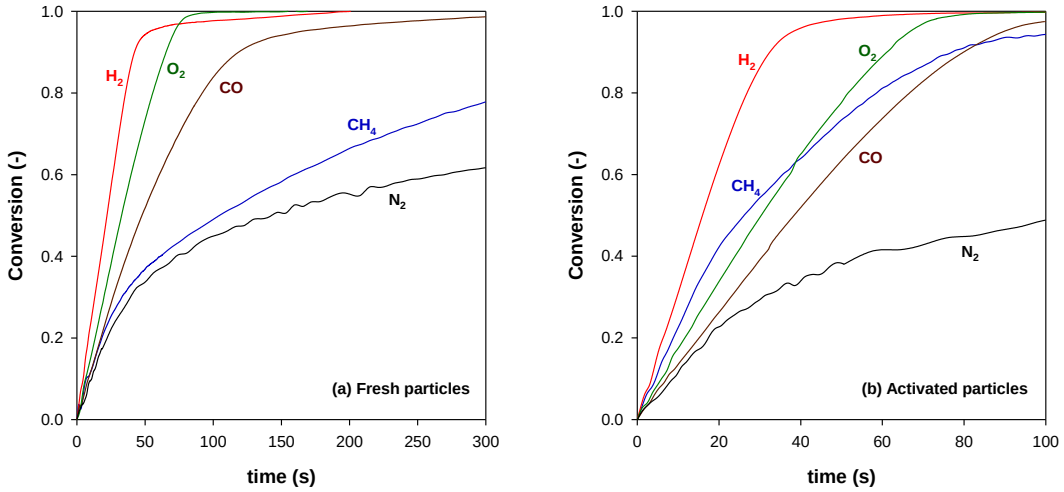

Fig. 4. Conversion vs. time curves during reduction period with CH_4, H_2 or CO and oxidation period by O_2 for (a) fresh particles and (b) activated particles. T = 1173 K; fuel: 15 vol.%; O_2: 10 vol.%.

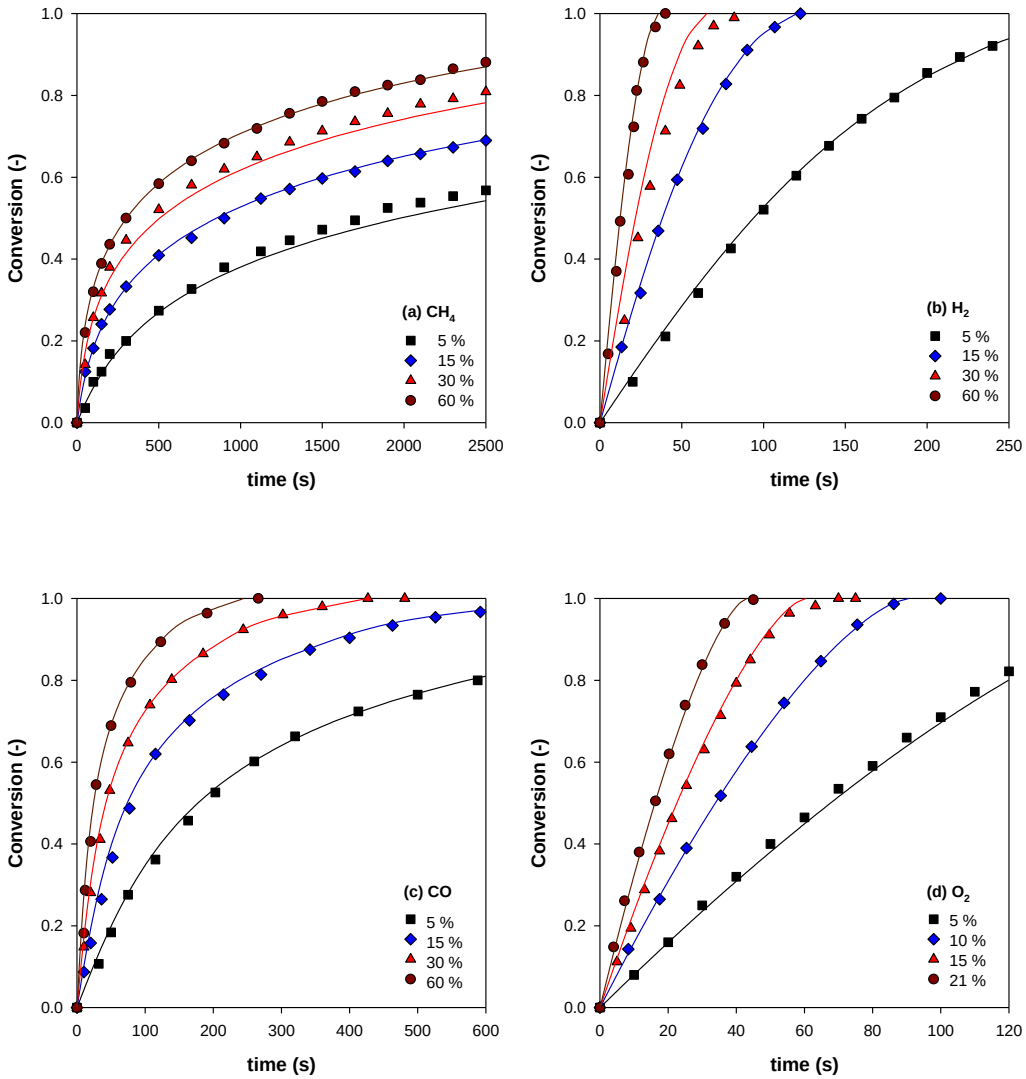

Fig. 5. Effect of gas concentration on the reaction rate of fresh particles with (a) CH_4; (b) H_2; (c) CO; and (d) O_2. T = 1073 K. Symbols: experimental curve. Continuous line: model predictions.

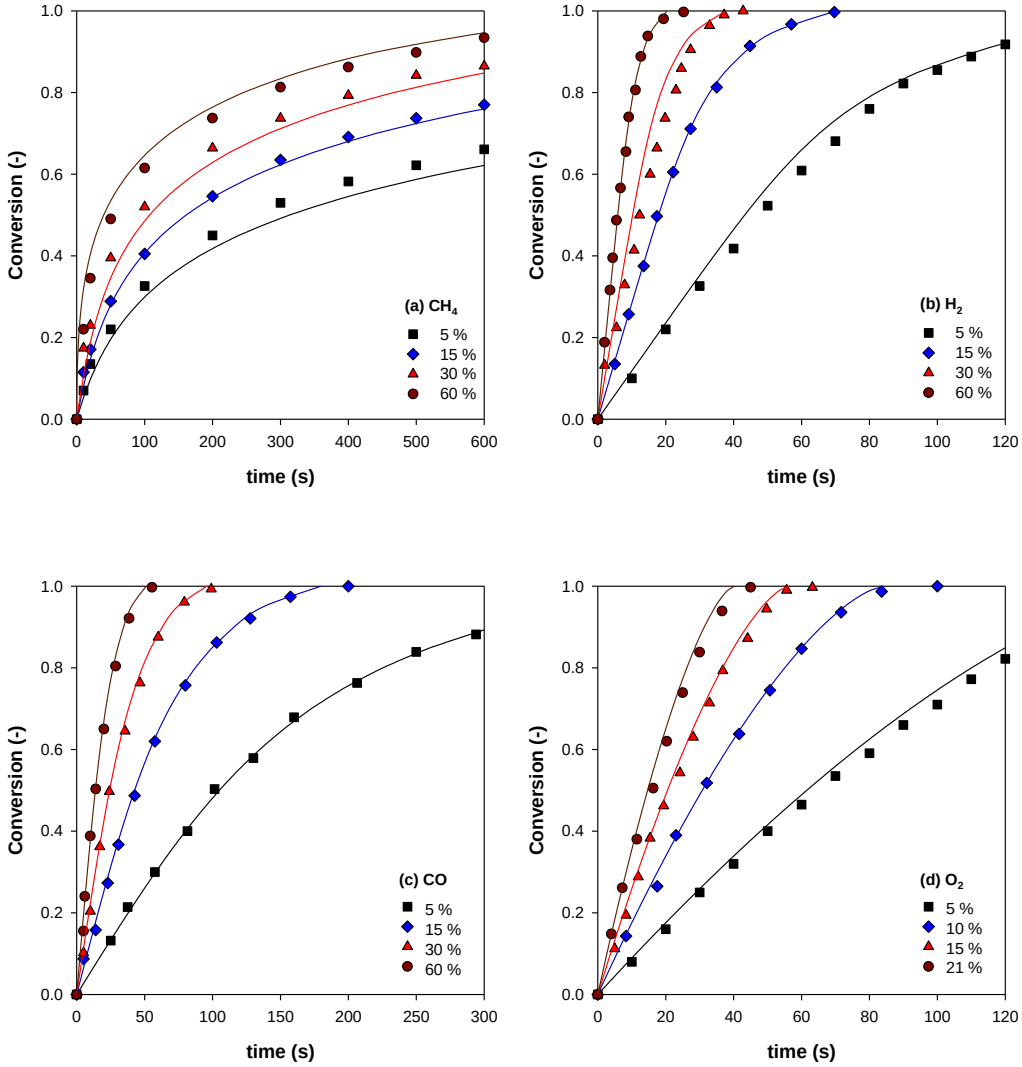

Fig. 6. Effect of gas concentration on the reaction rate of activated particles with (a) CH_4; (b) H_2; (c) CO; and (d) O_2. T = 1073 K. Symbols: experimental curve. Continuous line: model predictions.

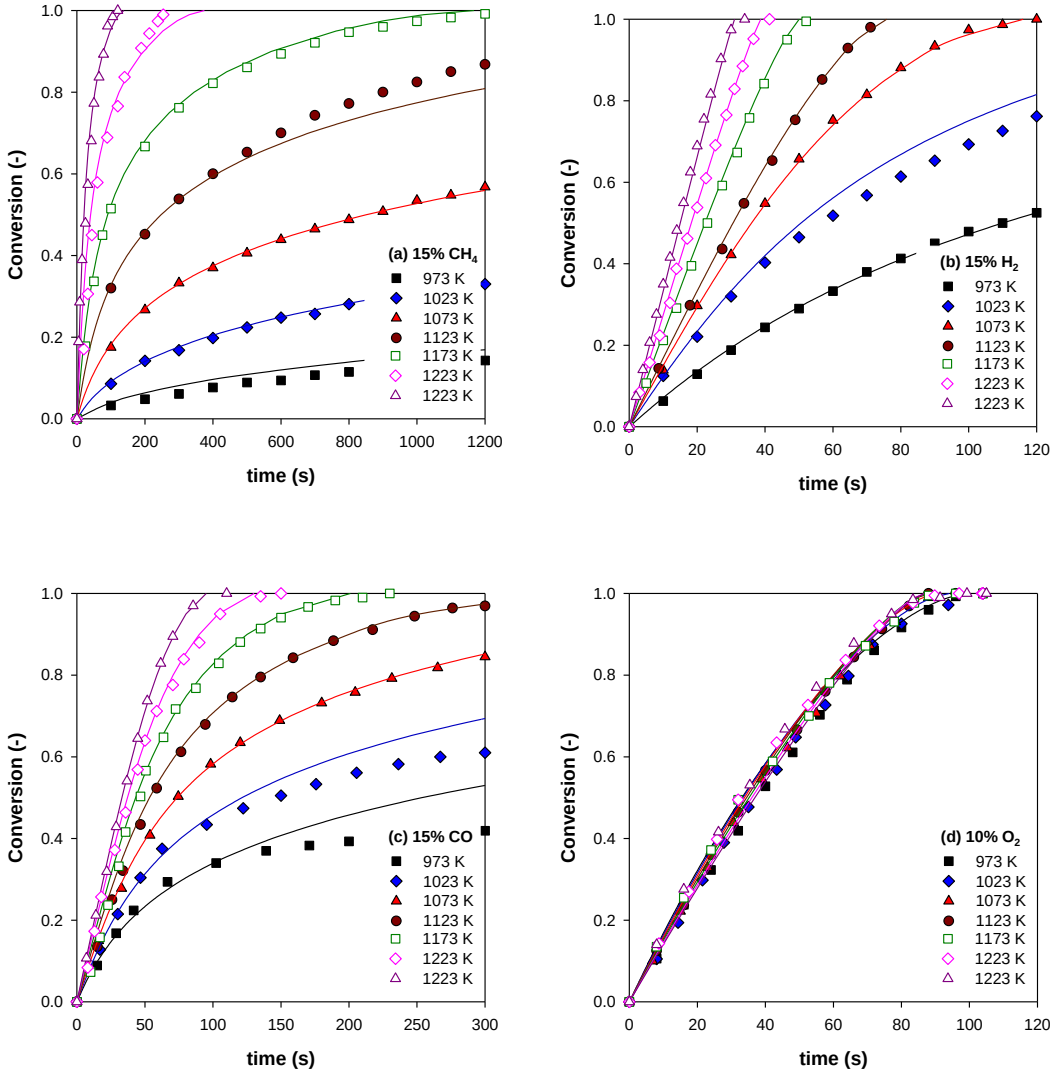

Fig. 7. Effect of temperature on the reaction rate of fresh particles with (a) CH_4; (b) H_2; (c) CO; and (d) O_2. 15 vol.% reducing agent or 10 vol.% O_2. Symbols: experimental curve. Continuous line: model predictions.

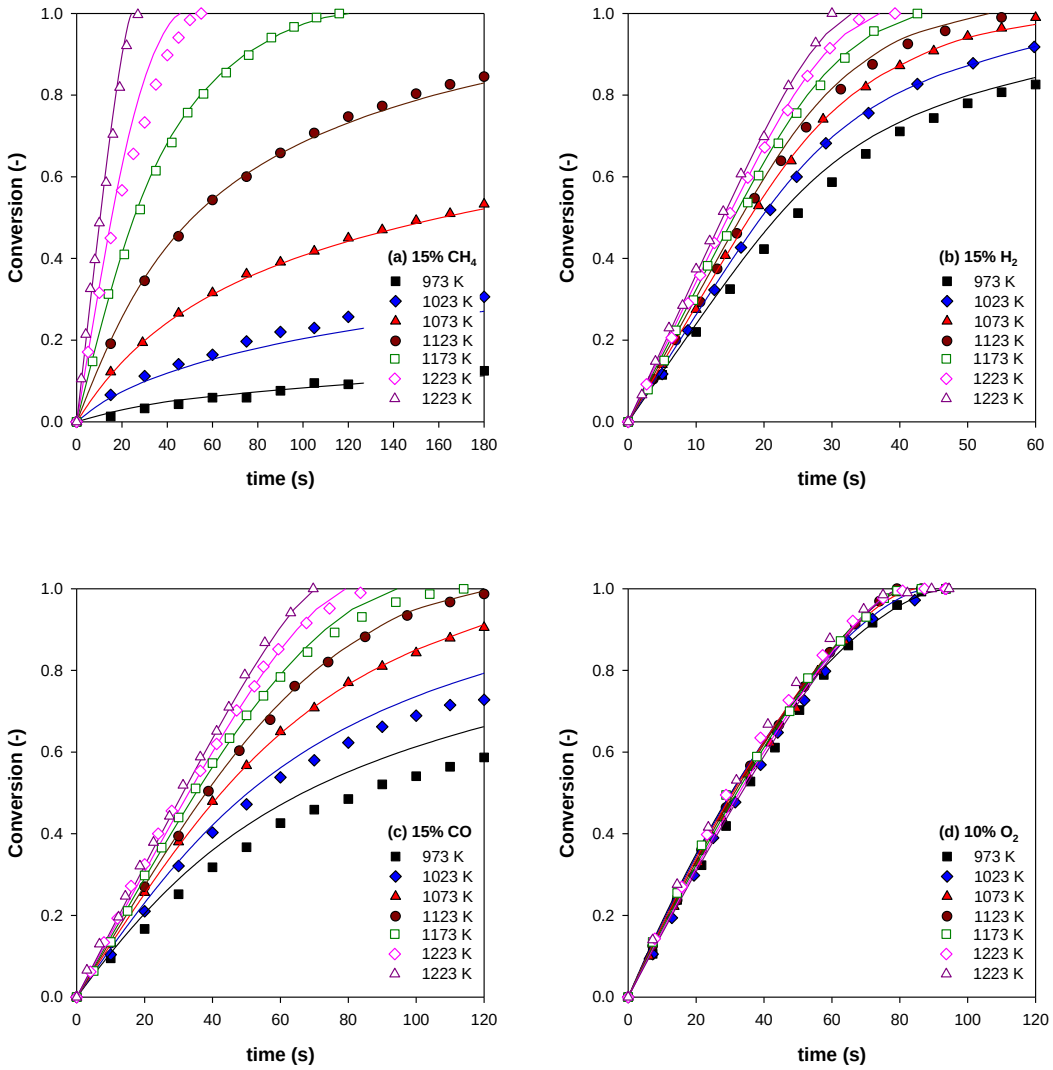

Fig. 8. Effect of temperature on the reaction rate of activated particles with (a) CH_4; (b) H_2; (c) CO; and (d) O_2. 15 vol.% reducing agent or 10 vol.% O_2. Symbols: experimental curve. Continuous line: model predictions.

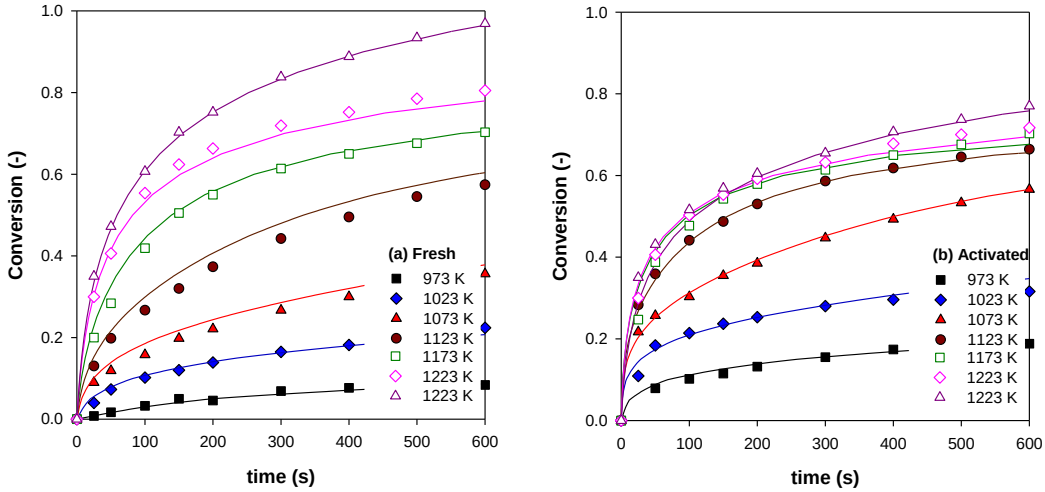

Fig. 9. Effect of temperature on the oxygen uncoupling reaction rate of (a) fresh and (b) activated particles in pure N_2. Symbols: experimental curve. Continuous line: model predictions.

Submitted, accepted and published by
Chemical Engineering Journal 2015, 269, 67-81

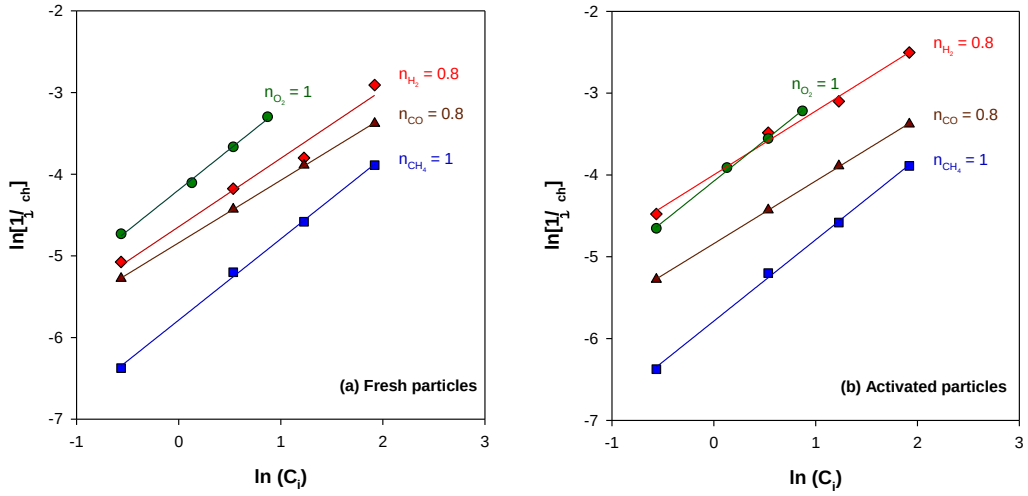

Fig. 10. Plot to obtain the reaction order with respect to CH_4, H_2, CO and O_2 for (a) fresh and (b) activated particles. T = 1073 K.

Submitted, accepted and published by
Chemical Engineering Journal 2015, 269, 67-81

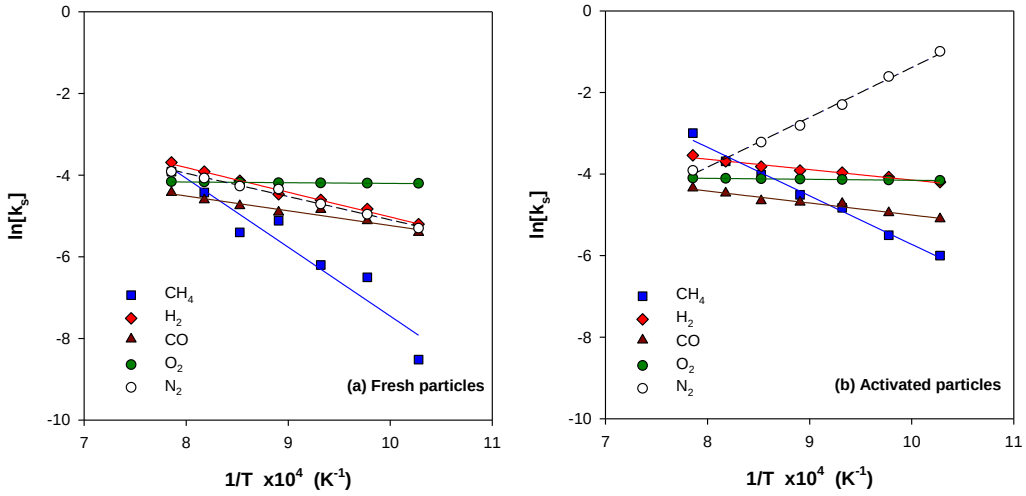

Fig. 11. Arrhenius plot for the kinetic constant k_s for the reaction of CH_4, H_2, CO and O_2 for (a) fresh and (b) activated particles. The kinetic constant values for oxygen uncoupling reaction in N_2 for fresh particles are also included.

Submitted, accepted and published by
Chemical Engineering Journal 2015, 269, 67-81

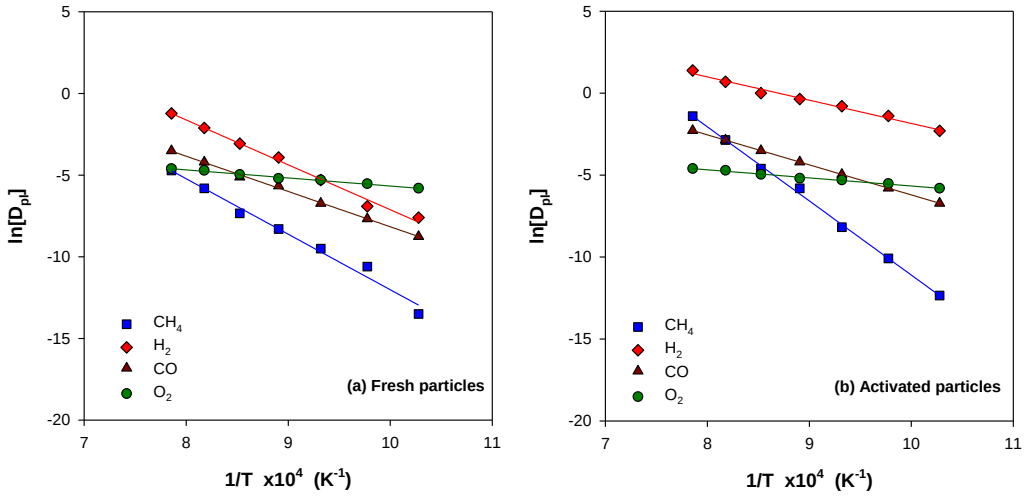

Fig. 12. Arrhenius plot for the effective diffusivity in the product layer D_{pl} for the reaction of CH_4, H_2, CO and O_2 for (a) fresh and (b) activated particles.

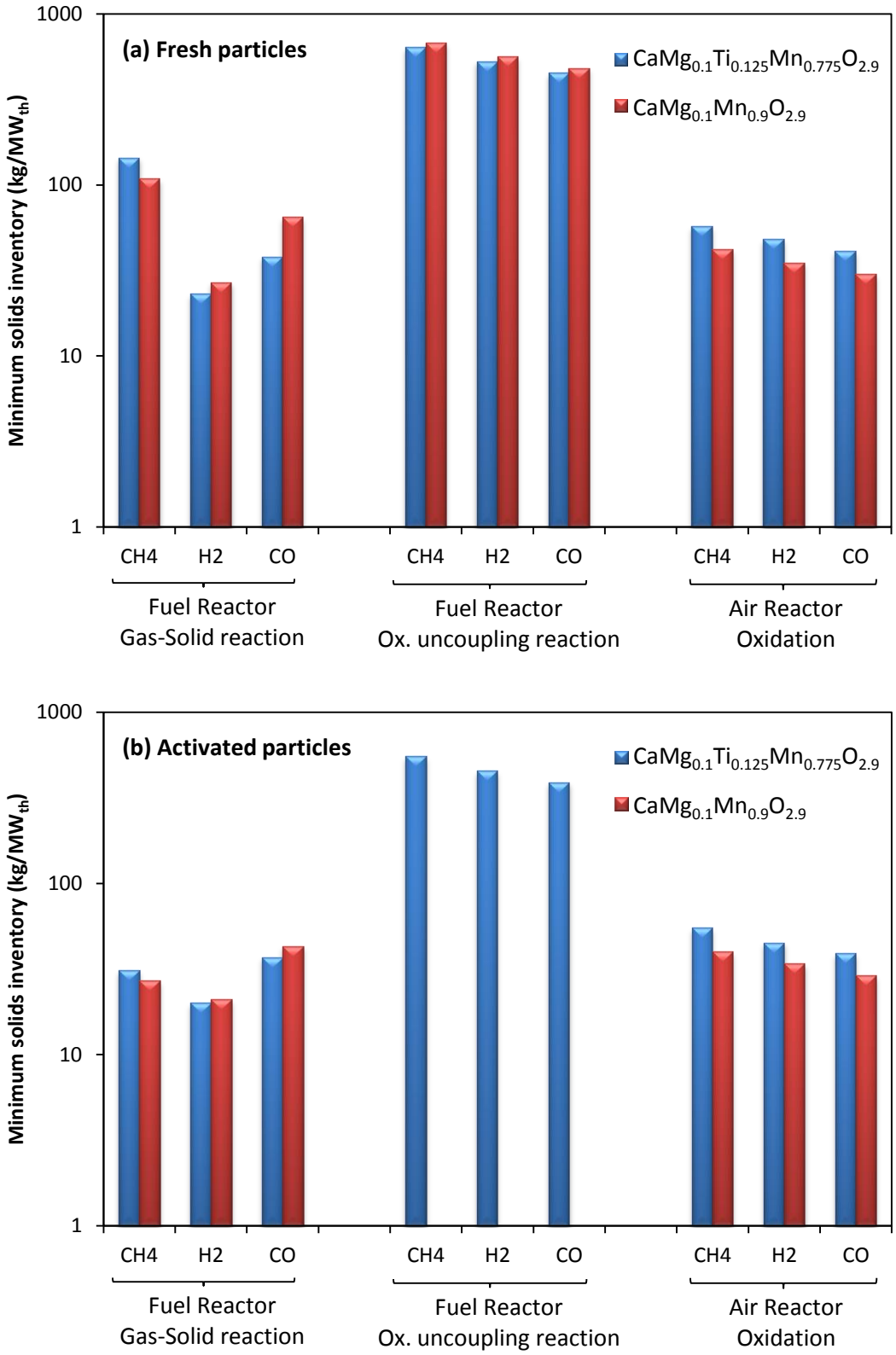

Fig. 13. Minimum solids inventory in the fuel and air reactors for $CaMg_{0.1}Ti_{0.125}Mn_{0.775}O_{2.9-\delta}$ following the method proposed in [37]. Values obtained for $CaMg_{0.1}Mn_{0.9}O_{2.9-\delta}$ are also presented for comparison purposes [27].

Submitted, accepted and published by
Chemical Engineering Journal 2015, 269, 67-81

Table 1. Kinetic parameters for reaction of fresh $CaMg_{0.1}Ti_{0.125}Mn_{0.775}O_{2.9-\delta}$ particles with CH_4, CO, H_2 and O_2, and oxygen uncoupling in N_2.

		units	CH_4	H_2	CO	O_2	N_2
n	Order of the reaction	-	1	0.8	0.8	1	0.7
$k_{s,0}$	Pre-exponential factor of k_s	$m^{3n}\ mol^{-n}\ s^{-1}$	$1.2 \cdot 10^{4}$	4.6	$2.1 \cdot 10^{-1}$	$1.8 \cdot 10^{-2}$	1.8
E_{ch}	Activation energy for k_s	kJ/mol	140.2	55.2	30.5	2.0	47.4
n'	Order of diffussion	-	0.7	1	0.8	1	-
$D_{pl,0}$	Pre-exponential factor of D_{pl}	$m^{3m}\ mol^{-n}\ s^{-1}$	$8.7 \cdot 10^{9}$	$7.2 \cdot 10^{8}$	$6.7 \cdot 10^{5}$	$5.0 \cdot 10^{-1}$	-
E_{pl}	Activation energy for D_{pl}	kJ/mol	291.9	228.8	179.4	41.1	-
$k_{x,0}$	Pre-exponential factor of k_X	-	2.0	1.0	2.0	0	-

Submitted, accepted and published by
Chemical Engineering Journal 2015, 269, 67-81

Table 2. Kinetic parameters for reaction of activated $CaMg_{0.1}Ti_{0.125}Mn_{0.775}O_{2.9-\delta}$ particles with CH_4, CO, H_2 and O_2, and oxygen uncoupling in N_2.

		units	CH_4	H_2	CO	O_2	N_2
n	Order of the reaction	-	0.4	0.8	0.8	1	1
$k_{s,0}$	Pre-exponential factor of k_s	$m^{3n}\ mol^{-n}\ s^{-1}$	$6.1 \cdot 10^{2}$	$2.0 \cdot 10^{-1}$	$9.8 \cdot 10^{-2}$	$2.0 \cdot 10^{-2}$	$1.2 \cdot 10^{-6}$
E_{ch}	Activation energy for k_s	kJ/mol	101.2	21.2	21.9	2.0	-101.5
n'	Order of diffussion	-	0.7	1	1	1	-
$D_{pl,0}$	Pre-exponential factor of D_{pl}	$m^{3m}\ mol^{-n}\ s^{-1}$	$6.4 \cdot 10^{14}$	$2.3 \cdot 10^{5}$	$1.8 \cdot 10^{5}$	$5.0 \cdot 10^{-1}$	-
E_{pl}	Activation energy for D_{pl}	kJ/mol	375.7	118.0	152.3	41.1	-
$k_{x,0}$	Pre-exponential factor of k_X	-	2.0	5.0	2.0	0	-